HOFMANN STABILITY CHARTS REVISITED FOR PIP-II: FROM CLASSICAL THEORY TO ASSUMPTION-FREE AND ML-DRIVEN MAPS

Abhishek Pathak*, Fermi National Accelerator Laboratory, Batavia, IL, USA

Abstract

The Hofmann stability chart remains the standard graphical tool for visualizing parametric resonances in space-charge–dominated linacs, but the published higher-order ($\ell = 3, 4$) dispersion relations are routinely used in the isotropic limit and the chart returns a binary stable/unstable verdict. We revisit the chart for the PIP-II linac along three complementary tracks within the smooth-focused Kapchinskij–Vladimirskij (KV) framework. (1) A validated higher-order anisotropic dispersion solver implements the full S^2 and S^4/S^6 blocks of Hofmann's Eqs. (36) and (41); an internal-consistency audit identifies the $(1\mp2\hat{\eta}^2/\alpha)$ factors on the α-coupling terms of the S^4 block of Eq. (36) that are required for the equation to reduce analytically to its own stated isotropic-limit closed form Eq. (37). (2) A probabilistic chart layer with ensemble Monte Carlo uncertainty bands wraps the deterministic solver on top of an engineering jitter budget consistent with the PIP-II Final Design Report. (3) A solver-labelled random-forest surrogate with isotonic post-hoc calibration approximates the deterministic chart with held-out expected calibration error $\leq 1\%$ and sub-millisecond inference. We bound chart-based claims to the perturbative validity domain $S^2 \lesssim 10$; under that bound, seven of 38 perturbative-valid PIP-II periods exhibit nonzero coherent growth, with the dominant new contributions coming from $\ell = 3$ modes lifted by the anisotropic correction. The three non-perturbative periods are deferred to the companion paper's lattice-periodic Floquet treatment [7].

INTRODUCTION

The PIP-II 800-MeV H$^-$ superconducting linac at Fermilab [1, 2], currently under construction as the proton driver for LBNF/DUNE, is the first CW-capable megawatt-class SRF proton linac in the United States. It accelerates a 2-mA average current through 119 individually powered cavities in five families (HWR, SSR1, SSR2, LB650, HB650) over 23 cryomodules and ~186 m. The design adopts a non-equipartitioned trajectory in which $\varepsilon_z/\varepsilon_x$ evolves freely from ~0.9 at injection to ~8.5 in the LB650 section, and the working point traces a path across the Hofmann $(\nu_z/\nu_x, \nu_x/\nu_{0x})$ plane that skirts the standard parametric resonance bands.

The conventional Hofmann analysis [3] addresses such a trajectory under restrictive assumptions: smooth focusing, a KV phase space [4], the $\ell = 2$ collective mode in the isotropic limit, zero incoherent tune spread, and a binary stable/unstable verdict. We address those limitations within the same smooth-focused KV framework along three tracks. Track 1 implements the higher-order anisotropic ($\ell = 2, 3, 4_e$) dispersion relations directly from Hofmann's Eqs. (36) and (41) with full S^4/S^6 blocks rather than their iso-limit reductions, and bounds chart-based claims to the perturbative validity domain $S^2 \lesssim 10$. Track 2 wraps the solver in an ensemble Monte Carlo loop to produce probabilistic margins. Track 3 trains a fast solver-labelled surrogate for online working-point screening. The full anisotropic transcription, derivation of the missing $(1\mp2\hat{\eta}^2/\alpha)$ factors, per-period PIP-II application, and the Floquet treatment of the three non-perturbative lattice periods are presented in the companion PRAB submission [7].

METHODOLOGY

Self-Consistent Parametrization

All three tracks share a common mapping from lattice variables (tune ratio $R \equiv \nu_z/\nu_x$; transverse tune depression $\eta \equiv \nu_x/\nu_{0x}$; emittance ratio $\varepsilon_z/\varepsilon_x$) to the Hofmann internal variables. Following Ref. [3],

$$\hat{\eta} = \sqrt{R/(\varepsilon_z/\varepsilon_x)}, \tag{1}$$

with the symmetry flip $\hat{\eta} \to 1/\hat{\eta}$ applied whenever $\hat{\eta} < 1$ to maintain $\hat{\eta} \geq 1$; the post-flip tune ratio is $R_{\text{eff}} = R$ before the flip and $1/R$ after, with $\alpha = 1/R_{\text{eff}}$. The dimensionless space-charge parameter is

$$S^2 = (1-\eta^2)(1+\hat{\eta})/(R_{\text{eff}}^2\,\eta^2), \tag{2}$$

with $S^2 = 0$ for $\eta \geq 1$. The growth rate in units of the zero-current transverse tune is $\gamma/\nu_{0x} = \sqrt{-s}\,G_{\text{scale}}$ with $G_{\text{scale}} = R\eta$ before the flip and η after, where $s < 0$ is an unstable root of the dispersion relation.

Track 1: Validated Higher-Order Dispersion Solver

For $\ell \geq 3$ the dispersion relation is

$$D_\ell(s) = (1+\hat{\eta})^\ell + S^2 \sum_{k\in\mathcal{P}_\ell} \frac{N^{(1)}_{\ell k}(\alpha,\hat{\eta})}{d_{\ell k}-s} + S^4 \sum_{(i,j)\in\mathcal{Q}_\ell} \frac{N^{(2)}_{\ell ij}(\alpha,\hat{\eta})}{(d_{\ell i}-s)(d_{\ell j}-s)} + \cdots = 0, \tag{3}$$

with $d_{\ell k}$ the squared pole frequencies and $N^{(1)}_{\ell k}, N^{(2)}_{\ell ij}$ the residues from Hofmann's $\ell = 3, 4$ Eqs. (36), (41), (45). We implement the full anisotropic S^2 block for $\ell = 2, 3, 4_e, 4_o$

---

* abhishek@fnal.gov
This work was produced by FermiForward Discovery Group, LLC under Contract No. 89243024CSC000002 with the U.S. Department of Energy, Office of Science, Office of High Energy Physics.

and the full anisotropic S^4/S^6 blocks of Eqs. (36) and (41); only the $\ell = 4_o$ S^4/S^6 block is retained in the isotropic-limit closed form Eq. (46). An internal-consistency audit identifies that the α-coupling terms of the S^4 block of Eq. (36) require the $(1\mp 2\hat{\eta}^2/\alpha)$ factors with the same structural form as Hofmann's S^2 block — otherwise Eq. (36) does not reduce analytically to its own stated iso-limit form Eq. (37). The algebraic identity that closes the reduction is $-(9-s)^2 + 6(1-s)(9-s) + 27(1-s)^2 = -32s(3-s)$; with the corrected factors the dispersion functions $D_{3,e}$ and $D_{4,e}$ reduce to Eqs. (37) and (42) at $\alpha = \hat{\eta} = 1$ to floating-point zero across $S^2 \in \{0.5, 1, 2, 5\}$ on a dense s grid. Roots of $D_\ell(s) = 0$ are located by grid plus bisection. The smooth-focused S^2 expansion is well-behaved for $S^2 \lesssim 10$; beyond that the $S^2/S^4/S^6$ partial sum is not a convergent representation of the dispersion function, and chart-based growth rates are formal rather than physical. We restrict chart-based PIP-II claims to the $S^2 \leq 10$ subset and defer the rest to the companion paper [7].

Track 2: Probabilistic Chart with Ensemble Monte Carlo Uncertainty

At each nominal point (R_0, η_0) we draw $N_{\rm mc} = 500$ Monte Carlo perturbations with current jitter 3%, mismatch 10%, emittance-ratio scatter 5%, and tune jitter 2% (an engineering jitter budget consistent with the PIP-II FDR, not a measured distribution), propagated through the higher-order solver. With $G_i \equiv \gamma_i/\nu_{0x}$ and Θ the Heaviside step function,

$$P(\text{unstable}\,|\,R_0, \eta_0) = \frac{1}{N_{\rm mc}} \sum_{i=1}^{N_{\rm mc}} \Theta(G_i - G_{\rm th}), \qquad (4)$$

with threshold $G_{\rm th} = 0.01$, replaces the binary verdict with a continuous robustness measure. An outer ensemble Monte Carlo loop of $B = 200$ resamples produces $P_{84} - P_{16}$ uncertainty bands on P itself.

Track 3: Solver-Labelled ML Surrogate

A surrogate that learns the deterministic Hofmann classification turns the chart into a near-instant lookup for working-point screens and online use. We assemble $N_s = 2 \times 10^4$ samples drawn over the chart-relevant range in $(R, \eta, \varepsilon_z/\varepsilon_x)$, labelled 1 when the Track 1 solver returns $\gamma/\nu_{0x} > 10^{-2}$ and 0 otherwise. We train six baselines (logistic regression, RBF-SVM, random forest, gradient boost, MLP, kNN) with 5-fold grouped cross-validation on 4×4 buckets in $(\varepsilon_z/\varepsilon_x, \eta)$ to suppress neighbour leakage. The best ranker is the random forest with ROC–AUC 0.987; an isotonic post-hoc calibration [6] brings the held-out expected calibration error to $\leq 1\%$. As a cross-distribution test, classifiers trained on a synthetic piecewise band-rule (the heuristic labelling commonly used in the literature) and tested against solver labels collapse to ROC–AUC ≈ 0.70 — the rule does not generalise to the deterministic chart.

RESULTS

Track 1: Higher-Order Anisotropic Stability Maps

Figure 1 shows the corrected $\ell = 2$, $\ell = 2, 3$, and $\ell = 2, 3, 4_e$ stability charts at $\varepsilon_z/\varepsilon_x = 5$ with Hofmann's published Fig. 10 instability boundaries (hand-digitised, 68 boundary points) overlaid as an external consistency check; the median distance between the digitised boundaries and the solver-flagged growth regions is 0.27 in (R, η). This comparison is qualitative, not a precision benchmark.

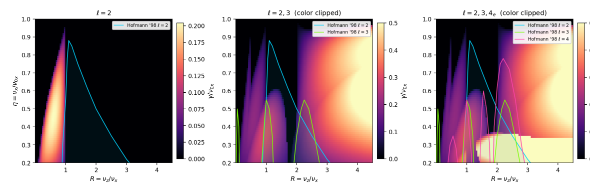

Figure 1: Corrected anisotropic stability charts at $\varepsilon_z/\varepsilon_x = 5.0$: cumulative mode sets $\ell = 2$, $\ell = 2, 3$, and $\ell = 2, 3, 4_e$, with Hofmann (1998) Fig. 10 instability boundaries overlaid (colour: $\ell = 2$ cyan, $\ell = 3$ green, $\ell = 4_e$ magenta) for external consistency.

Table 1 summarises the section-level maxima along the PIP-II trajectory after the anisotropic correction, with a separate column restricted to the perturbative-valid subset $S^2 \leq 10$. Three periods sit outside that subset — SSR1 idx 8 at $S^2 = 21$, SSR1 idx 12 at $S^2 = 65$, and SSR2 idx 26 at $S^2 = 18$ — and produce formal growth rates that we exclude from quantitative chart-based claims; their quantitative interpretation is deferred to the companion paper's Floquet analysis [7]. Within the 38 perturbative-valid periods, seven exhibit nonzero coherent growth above $G_{\rm th}$, with the largest contributions at LB650 idx 33 ($\ell = 3$, $\gamma/\nu_{0x} = 0.24$) and SSR1 idx 15 ($\ell = 3$, 0.22); both are lifted by the anisotropic correction relative to the iso-limit, and removing the correction returns the previous five-period count from $\ell = 2$ alone.

Table 1: Section-level peak γ/ν_{0x} along the PIP-II trajectory after the anisotropic correction. "all" is the all-period maximum; "valid" restricts to $S^2 \leq 10$. † marks sections containing one or more non-perturbative periods.

Section	N_p	ℓ=2	ℓ=3	ℓ=4_e	all	valid
HWR	8	0.09	0.00	0.00	0.09	0.09
SSR1†	8	0.11	0.22	0.45	0.45	0.22
SSR2†	12	0.00	0.27	0.00	0.27	0.00
LB650	9	0.15	0.24	0.00	0.24	0.24
HB650-1	1	0.00	0.00	0.00	0.00	0.00
HB650-2	3	0.07	0.00	0.05	0.07	0.07

Track 2: Probabilistic Margins

Figure 2 shows the probabilistic chart at $\varepsilon_z/\varepsilon_x = 5.73$. The $P = 0.5$ contour lies $\Delta\eta \approx 0.10$–0.15 above the deterministic boundary; the $P \in [0.1, 0.9]$ transition band spans $\Delta\eta \approx 0.15$–0.20. The 68% MC uncertainty band $P_{84} - P_{16}$

peaks at ≈ 0.05, indicating that the probability contours are stable against ensemble resampling. The PIP-II trajectory occupies $P \approx 0$ for the majority of the 38 perturbative-valid periods.

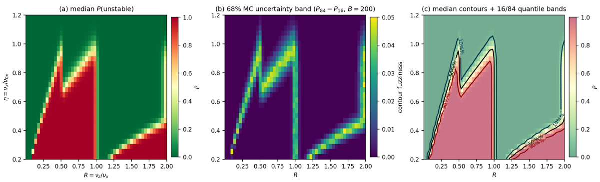

Figure 2: Probabilistic chart at $\varepsilon_z/\varepsilon_x = 5.73$, $N_{\mathrm{mc}} = 500$ inner draws, $B = 200$ ensemble resamples. (a) median P(unstable). (b) 68% MC uncertainty band $P_{84} - P_{16}$. (c) $P = 0.1, 0.5, 0.9$ contours overlaid on the median surface.

Track 3: ML Surrogate Performance

The random forest with isotonic post-hoc calibration on solver labels achieves accuracy 0.94, ROC–AUC 0.987, and held-out expected calibration error $\leq 1\%$; single-core inference is $\sim 30\ \mu$s per point versus seconds for the deterministic solver. The cross-distribution test — training on the legacy piecewise band-rule and evaluating against solver labels — collapses to ROC–AUC ≈ 0.70, a sharp indication that the heuristic rule is not a substitute for the corrected deterministic chart. Operationally the calibrated random forest serves as a fast screening pass for working-point selection; quantitative interpretation of any flagged point remains anchored to Track 1.

CONCLUSION

A corrected higher-order anisotropic Hofmann solver, a probabilistic margin layer with ensemble Monte Carlo uncertainty, and an isotonic-calibrated solver-labelled ML surrogate together provide a layered margin picture for PIP-II within the perturbative validity domain $S^2 \lesssim 10$. Seven of 38 perturbative-valid PIP-II periods exhibit nonzero coherent growth, dominated by anisotropy-induced $\ell = 3$ contributions absent from the iso-limit treatment (LB650 idx 33 at $\gamma/\nu_{0x} = 0.24$, SSR1 idx 15 at 0.22). The three non-perturbative periods (SSR1 idx 8, SSR1 idx 12, SSR2 idx 26) sit outside the perturbative domain and are deferred to the companion paper's lattice-periodic Floquet analysis [7]. The workflow ports directly to other smooth-focused KV-modelled SRF proton or H^- linacs.

REFERENCES

[1] M. Ball *et al.*, "The PIP-II conceptual design report," Fermilab, Batavia, IL, USA, Rep. FERMILAB-DESIGN-2017-01, Mar. 2017.

[2] A. Pathak, A. Saini, and E. Pozdeyev, "Final physics design of proton improvement Plan-II at Fermilab,"in *Proc. IPAC'24*, Nashville, TN, USA, May 2024, pp. 125–128. doi:10.18429/JACoW-IPAC2024-MOPC30

[3] I. Hofmann, "Stability of anisotropic beams with space charge,"*Phys. Rev. E*, vol. 57, no. 4, pp. 4713–4724, Apr. 1998. doi:doi:10.1103/PhysRevE.57.4713

[4] I. M. Kapchinskij and V. V. Vladimirskij, "Limitations of proton beam current in a strong focusing linear accelerator," in *Proc. Int. Conf. on High-Energy Accelerators and Instrumentation (HEACC'59)*, Geneva, Switzerland, Sep. 1959, p. 274.

[5] D. Uriot and N. Pichoff, TraceWin, CEA Saclay, France. https://www.dacm-logiciels.fr/tracewin

[6] F. Pedregosa *et al.*, "Scikit-learn: machine learning in Python," *J. Mach. Learn. Res.*, vol. 12, pp. 2825–2830, Oct. 2011. https://jmlr.org/papers/v12/pedregosa11a.html

[7] A. Pathak, "Hofmann stability charts revisited for high-power linacs: higher-order modes, probabilistic margins, and a solver-labelled surrogate, with application to PIP-II," submitted for publication.